

Efficient degradation of phenol and 4-nitrophenol by surface oxygen vacancies and plasmonic silver co-modified Bi₂MoO₆ photocatalysts

Huidong Shen,^{[a]†} Wenwen Xue,^{[a]†} Feng Fu,^{*[a]} Jiefang Sun,^[b,c] Yanzhong Zhen,^[a] Danjun Wang,^{*[a]} Bing Shao,^{*[c]} and Junwang Tang^{*[b]}

Abstract: In this work, we rationally combined the surface plasmon resonance effect of metallic Ag, surface oxygen vacancies and Bi₂MoO₆ photocatalyst together to construct novel oxygen vacancy-rich Ag/Bi₂MoO₆ (A/BMO-SOVs) photocatalysts and further investigated its synergistic effect on photocatalytic degradation of phenol and 4-nitrophenol under visible light irradiation ($\lambda \geq 420$ nm). TEM, EPR and Raman spectra demonstrated the co-existence of metallic Ag nanoparticles, surface oxygen vacancies and Bi₂MoO₆ due to a controlled calcination process. The experiment results disclosed that the 2%A/BMO-SOVs-375 sample exhibited the highest photocatalytic activity for the degradation of both phenol and 4-nitrophenol under visible light irradiation, achieving nearly 100% and 80% removal efficiency, respectively, and demonstrating the apparent reaction rate constants ($k_{app, min^{-1}}$) of 183 and 26.5 times higher than that of pure Bi₂MoO₆, respectively. The remarkable photodegradation performance of A/BMO-SOVs for organic substance was attributed to the synergistic effect between the surface oxygen vacancies, metallic Ag nanoparticles and Bi₂MoO₆, which not only improves the visible light response ability, but also facilitates charge separation. Thus this work provides an effective strategy for the design and fabrication of highly efficient photocatalysts through integrating surface oxygen vacancies and surface plasmon resonance effect of nanoparticles, which has a potential to both water treatment and air purification.

Introduction

In recent years, semiconductor-based photocatalysis has been regarded as one of the most promising technologies to address the environmental contamination because it can completely

decompose organic pollutants into carbon dioxide and H₂O.^[1-4] From the viewpoint of solar energy utilization, it is desirable to develop highly active and environment friendly visible-light-driven photocatalysts to meet the requirements of potential industrial applications.^[5-6] Among various semiconductor photocatalysis, bismuth-based semiconductor materials have attracted extensive attention over the past few years owing to their less toxicity, suitable band positions and photoresponse to the visible region.^[7,8] Among these bismuth-based compounds, Bi₂MoO₆ is a simplest member of the Aurivillius-type compounds, which is made up of alternate [Bi₂O₂]²⁺ layers and MoO₄²⁻ perovskite layers.^[9] Recently, some studies have clearly revealed that Bi₂MoO₆ might be a promising candidate as an excellent photocatalyst owing to a series of advantages, e.g. high chemical durability, non-toxic, naturally abundant, and an appropriate band gap (2.5-2.8 eV).^[10,11] This material has generally been used in many fields including Li-ion batteries, water splitting, hydrogen energy, and organic pollutant degradation.^[12-16] Nevertheless, pure Bi₂MoO₆ suffers from low visible light utilization efficiency, the relatively rapid recombination of photoexcited electron-hole pairs, and slow carrier transport, which limit its practical application.^[17,18] Therefore, to further extend the visible light response region and improve the photocatalytic activity of Bi₂MoO₆-based materials are highly challenging while appealing.

In order to achieve such goal, the introduction of oxygen vacancy on the semiconductor surface is proposed. It is widely recognized that surface oxygen vacancies (SOVs) would play an critical role in photocatalytic process, especially in terms of the photo-catalytic degradation of pollutants,^[19] owing that they can narrow down the band gaps of semiconductors and tailor their electronic structures.^[20] Recently, some studies clearly demonstrated that the introduction of SOVs within semiconductor photocatalysts not only extended the visible light response region, but also accelerated the separation of photogenerated electrons and holes, leading to high photocatalytic activity.^[21-24] For example, Lv and co-workers reported that the introduction of SOVs in BiPO₄ via controllable hydrogen reduction,^[25] and the presence of oxygen vacancies in BiPO₄ resulted in broadening the valence band width and narrowing the band gap, thus leading to an extended photoresponse wavelength range and enhanced photocatalytic performance. Recently, Yu and co-workers also introduced oxygen vacancies into Bi₂O₂CO₃ via a facile and scalable precipitation approach with assistance of glyoxal as reductant, and further confirmed the favorable effect of oxygen vacancies on extending the visible light response region and accelerating the separation of photo-generated electrons and holes.^[26]

[a] H.D. Shen, W.W. Xue, Prof. Dr. F. Fu, Y.Z. Zhen, Prof. Dr. D.J. Wang
Shaanxi Key Laboratory of Chemical Reaction Engineering, College
of Chemistry and Chemical Engineering
Yan'an University
Yan'an 716000, P. R. China
E-mail: yadxufufeng@126.com; wangdj761118@163.com;
shaobingch@sina.com; junwang.tang@ucl.ac.uk

[b] Dr J.F. Sun, Prof. Dr. J.W. Tang
Department of Chemical Engineering
University College London
Torrington Place, London WC1E 7JE, UK.

[c] Dr J.F. Sun, Prof. Dr B. Shao
Beijing Center for Diseases Prevention and Control
Beijing 100013, P. R. China.

† These authors contributed equally to this work.

Supporting information for this article is given via a link at the end of the document.

Therefore, it is sought-after to introduce the SOVs in the Bi₂MoO₆-based materials to extend its visible light response region and improve the photocatalytic activity.

Recent results revealed that noble metal (Au, Ag etc.) decoration of photocatalysts is another effective approach to improving the photocatalytic performance owing to strongly localized surface plasmonic resonance (SPR) effect,^[27-29] which can extend the visible light response region and enhance the separation of the photogenerated charge carriers of photocatalysts.^[30] In addition, Schottky junctions at the interface between noble metal nanoparticles and semiconductors might effectively promote transfer of electrons, thereby to some extent inhibiting the recombination rates of photogenerated electrons and holes.^[31] Among these metal nanoparticles, Ag nanoparticles are relatively low-cost and widely employed to augment the photocatalytic activity of semiconductor. For example, Chen and co-workers prepared Ag nanoparticle decorated zinc oxide nanostructures, and found that the nanoparticulate composites possessed enhancement in photocatalytic performance for the oxidization of methane.^[32] Wang and co-workers used a facile impregnation-roasting method to prepare Ag/g-C₃N₄ composite.^[33] The obtained Ag/g-C₃N₄ composite exhibited high photocatalytic activities toward aerobic oxidative amidation of aromatic aldehydes under visible light irradiation owing to strongly LSPR effect of Ag. Recently, Di and co-workers reported that the Ag quantum dots were deposited onto the surface of BiOBr nanosheets to generate a heterostructured Ag/BiOBr metal-semiconductor with an enhanced photocatalytic performance.^[34]

To achieve an optimal photocatalytic activity, the combination of above-mentioned two strategies is applied to the preparation of a heterostructured photocatalyst.^[35-38] To our knowledge, such a design strategy for the visible driven Bi₂MoO₆-based photocatalytic materials has seldom been reported yet. Herein, inspired by the above impressive advances, in this work, we have rationally designed and successfully fabricated a novel oxygen vacancy-rich Ag/Bi₂MoO₆ photocatalysts with a high visible light driven photocatalytic activity via a facile solvothermal methods combined with impregnation-calcination approach. Phenol and 4-nitrophenol (4-NP) were used as probe organic pollutants to assess the photocatalytic activities of the prepared samples. Moreover, the reaction parameters for phenol removal have been systematically studied, such as calcination temperatures, calcination time, metallic Ag contents and the dosage of photocatalysts. The experiment results disclosed that the obtained 2%A/BMO-SOVs-375 exhibited the highest photocatalytic activity for the degradation of phenol and 4-nitrophenol under visible light irradiation, in which the apparent reaction rate constants (k_{app}/min^{-1}) are 183 and 26.5 times higher than that of pure Bi₂MoO₆. The highly enhanced photocatalytic efficiency observed in A/BMO-SOVs should be attributed to the synergistic effect of the SOVs and SPR metallic Ag. This work has been proven to be a new strategy, which is also applicable to the design and fabrication of other photocatalytic systems to enhance photocatalytic performance.

Scheme 1. Schematic illustration of the preparation process of A/BMO-SOVs samples.

Results and Discussion

Structure and morphology characterization

The crystalline phase of as-obtained samples was investigated by XRD analysis, and the results were displayed in Figure 1a. It is clear to see that the BMO and 2%A/BMO-SOVs-375 composites show the same diffraction peaks, which can be indexed to orthorhombic BMO (JCPDS card No.76-2388), indicating that low content of Ag added and low temperature calcination have no obvious influence on the crystalline structure of BMO (Figure 1a). It should be noted that no obvious diffraction peaks of Ag are observed, which might be attributed to the low loading amount, small particle size, good dispersion and the dominant peaks of BMO in the obtained samples.^[39] However, for the patterns of 2%A/BMO-SOVs-375 (PD) and 2%A/BMO (PD), the intensity of diffraction peaks were severely weakened, which might be attributed to the XRD signals partially covered by Ag nanoparticles.^[33] As can be seen from Figure 1b, with increasing calcination temperature, the (131) diffraction peak slightly shifts to a higher 2Theta angle in the amplifying XRD patterns due to high temperature-induced the displacement of oxygen atoms, resulting in lattice distortion and oxygen vacancies.^[40] Figure S1a shows the XRD patterns of 2%A/BMO-SOVs prepared at various calcination temperatures. It was found that no impurity phase was formed when calcination temperatures were below 375 °C. However, when the temperature reached 450 °C, it was found that characteristic peaks of metallic Ag marked with solid triangle appeared, which agree well with face centered cubic Ag corresponding to JCPDS files No. 04-0783 (Figure S1b), while peaks marked with solid tetragonum agree well with monoclinic AgO corresponding to JCPDS files No. 89-3081, which is due to the calcination in air.

To further confirm the co-existence of Ag nanoparticles and surface defects, XPS spectra of the as-obtained BMO and A/BMO-SOVs were performed. The survey XPS curve in Figure S1c clearly reveals that the 2%A/BMO-SOVs-375 composite mainly composed of Bi, Mo, O and Ag elements. Figure 1c and 1d present the high resolution spectra of Bi 4f and O 1s for the BMO and 2%A/BMO-SOVs-375 samples. As shown in Figure 1c, two asymmetric peaks located at 159.3 eV and 164.3 eV belong to the binding energy of Bi 4f_{7/2} and Bi 4f_{5/2}, respectively, suggesting that the Bi is in the form of Bi³⁺. The corresponding peaks in the spectra of 2%A/BMO-SOVs-375 shifted to 159.4 and 164.7 eV, respectively, being 0.1 eV higher than those of BMO, thus implies the existence of SOVs and the strong interaction between Ag and BMO. As presented in Figure S1d, two characteristic peaks of Mo 3d_{5/2} and Mo 3d_{3/2} from Mo⁶⁺ respectively centered at 232.5 and 235.6 eV are observed. The asymmetric O 1s peak could be deconvoluted into three peaks at 529.8, 530.6, and 531.9 eV (Figure 1d), which are ascribed to the Bi-O, Mo-O, and OH group on the surface of BMO, respectively.^[41] However, the O 1s XPS spectra of 2%A/BMO-SOVs-375 shifted to a higher binding energy from 530.20 eV to

530.48 eV (Figure 1d), which is attributed to the formation of neighboring oxygen vacancies with a high electron-attracting effect.^[42] The XPS Ag 3d spectrum of 2%A/BMO-SOVs-375 is shown in Figure S1e, in which the two main peaks observed at 367.7 and 373.7 eV are ascribed to the binding energy of Ag 3d_{5/2} and Ag 3d_{3/2}, respectively, and the result is in accordance with previous reports.^[43] The above XPS analysis demonstrated that the 2%A/BMO-SOVs-375 nanocomposite was successfully obtained.

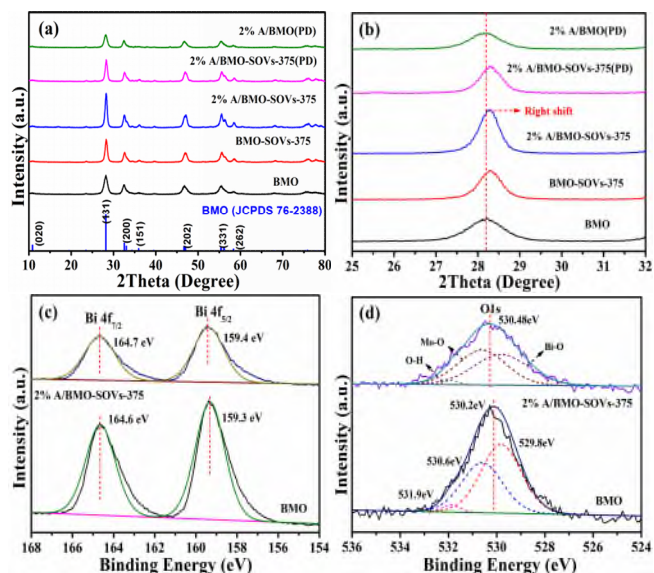


Figure 1. (a) XRD patterns of samples BMO, BMO-SOVs-375, 2%A/BMO-SOVs-375, 2%A/BMO-SOVs-375 (PD) and 2%A/BMO (PD), (b) XRD patterns in a 2Theta range of 25°-32°, XPS spectra of (c) Bi 4f and (d) O 1s for samples BMO and 2%A/BMO-SOVs-375.

The morphology and microstructure of as-obtained samples were revealed using SEM technology and the results were illustrated in Figure 2. Figure 2a and 2b show that the pure BMO sample is composed of well dispersed hierarchical microspheres with average diameter of 1-2 μm , which are assembled with a large amount of nanosheets with a thickness of 20-50 nm (inset of Figure 2b). As seen from Figure 2c and 2d, the morphology of 2%A/BMO-SOVs-375 sample inherit the similar hierarchical structure of BMO sample, indicating that the calcination processes does not obvious changes the morphology and size of BMO. However, compared to pure BMO, the surface of the prepared 2%A/BMO-SOVs-375 nanocomposites becomes blurred and disordered, which indicates the surface structure is damaged and SOVs are formed. In addition, some small spherical Ag nanoparticles are observed on the surface of the BMO hierarchical microspheres (inset of Figure 2d), indicating a high dispersion of Ag nanoparticles. Furthermore, to further analysis of elemental distribution on the 2%A/BMO-SOVs-375 sample, the corresponding EDS mapping were also performed. As shown in Figure 3a-3d, the Bi, Mo, O, and Ag elements are all detected and uniformly dispersed, which gives a very clear signal that the Ag nanoparticles are successfully loaded on the

surface of BMO after the impregnation-calcination procedure. This finding is in good agreement with the XPS results.

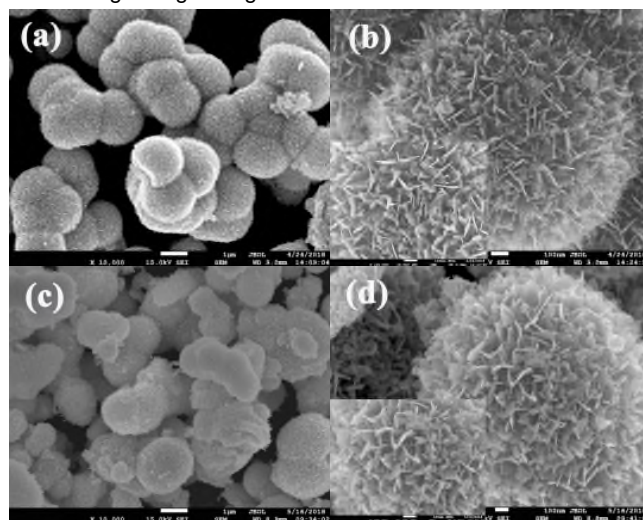


Figure 2. FE-SEM images of as-prepared (a, b) BMO, and (c, d) 2%A/BMO-SOVs-375 composites.

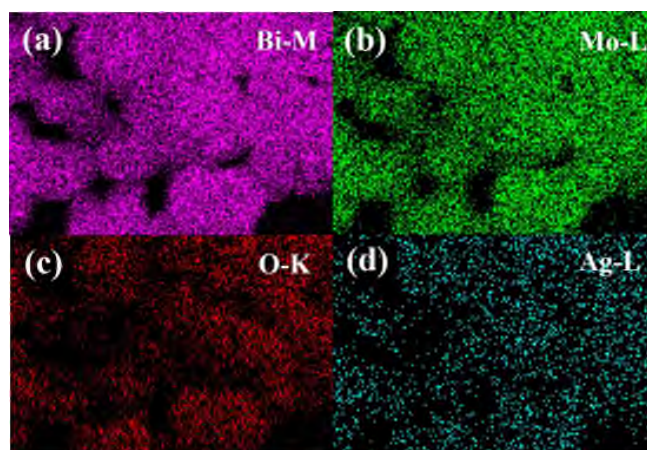


Figure 3. The corresponding EDS elemental mapping images of (a) Bi, (b) Mo, (c) O and (d) Ag in sample 2%A/BMO-SOVs-375.

For further investigating the morphological and structural characteristics of BMO and 2%A/BMO-SOVs-375, TEM and HRTEM analysis were carried out and the result is shown in Figure 4. Figure 4a and 4c show the TEM images of BMO and 2%A/BMO-SOVs-375, which revealed a hierarchical microspheres structure. Figure 4b revealed the HRTEM images of BMO. It can be clearly observed that the lattice spacing is measured to be 0.315 nm, which corresponds to the (131) crystal plane of BMO (inset of Figure 4b).^[44] Figure 4d shows the HRTEM image of 2%A/BMO-SOVs-375. It can be clearly indicates that the Ag nanoparticles were located on the surface of BMO (the red dotted line mark). Besides, the lattice fringe spacing of 0.236 nm can be observed on the surface, which matched with the (111) crystal plane of metal Ag (inset of Figure

4d).^[32, 39] The results demonstrated that metallic Ag was successfully loaded on the surface of BMO microspheres, which promoted the effective electrons and holes separation.

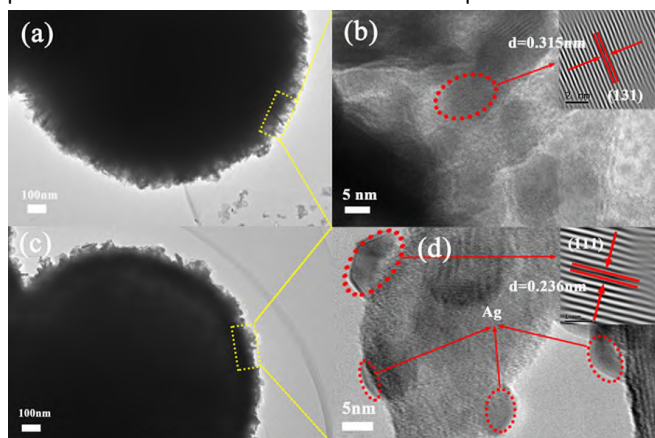


Figure 4. TEM and HR-TEM images of (a, b) BMO and (c, d) 2%A/BMO-SOVs-375 composites.

Formation of Surface Oxygen Vacancy

As shown in Figure 5a and 5b, the HRTEM image clearly reveals that both BMO and BMO-SOVs-375 are highly crystalline structure. However, it can see clearly that pure BMO sample displays a perfect lattice feature, while the edge of lattice fringe for BMO-SOVs-375 appears a disordered layer of about 2.794 nm thick. This phenomenon indicates the surface structure is damaged and maybe SOVs are formed. Hence, the generation of SOVs stems from the calcination process.

To provide a direct and solid evidences for the existence of oxygen vacancies, EPR spectra analysis was carried out. It has been reported that EPR can be directly and accurately detect the presence of oxygen vacancies in semiconductors.^[45] Figure 5c shows the EPR spectra of BMO, BMO-SOVs-375, and 2%A/BMO-SOVs-375. It can be found that only very weak EPR signal with a small g-value of 1.991 can be observed for BMO, which could be ascribed to the existence of oxygen vacancies.^[40] Compared to BMO, a strong symmetric peaks centered at g value of around 2.004 for BMO-SOVs-375 and 2%A/BMO-SOVs-375 were observed, which are typical peaks of surface oxygen vacancies.^[46, 47] In addition, it can be easily seen that the intensity of EPR signal for 2%A/BMO-SOVs-375 is considerably stronger than that of BMO-SOVs-375, which was gradually enhanced with increasing SOVs' concentration.^[48] This result further corroborates that the successful formation of oxygen vacancies on BMO surface via a facile impregnation-calcination methods.

In order to further investigate the crystal defects and the distortion of crystal structure, Raman spectroscopy were performed and the results were illustrated in Figure 5d. It was found that pure BMO exhibited many characteristic peaks at 138, 282, 351, 399, 714, 798 and 844 cm^{-1} (Figure 5d). The characteristic peaks at 714, 798 and 844 cm^{-1} were correspond to the asymmetric, symmetric and asymmetric stretching

vibrations of the MoO_6 octahedrons, respectively.^[49] Additionally, the characteristic peaks below 400 cm^{-1} can be attributed to both Bi-O stretches and lattice modes, which is in good accordance with previous report.^[50] From the Raman vibrations of the BMO-SOVs-375, it show the similar Raman vibration modes. Furthermore, the vibrating peaks of BMO-SOVs-375 is stronger than BMO, indicating that the BMO-SOVs-375 contain more MoO_6 octahedral structures. The increase in the intensities of these vibrational modes for the calcined samples suggested the deformation of the crystal structure after calcination, which could be attributed to the contribution of surface oxygen vacancies.^[51] Compared with BMO, the characteristic peaks of 2%A/BMO-SOVs-375 and 2%A/BMO (PD) display an enhancement of peak intensity, which is attributed to the strong interaction between metal Ag and BMO interface as well as the energy coupling process to enhance the Raman signals.^[52] Based on the results from TEM, EPR, and Raman spectra analyses, both SOVs and metallic Ag were successfully produced on the A/BMO-SOVs via a reliable calcination process.

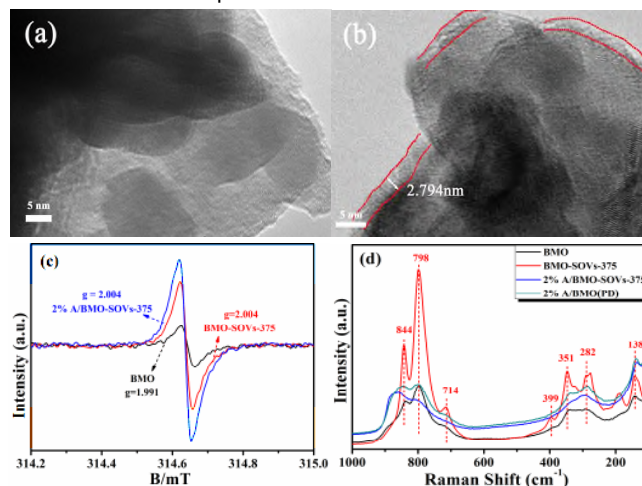


Figure 5. HR-TEM images of (a) BMO and (b) BMO-SOVs-375, (c) EPR spectra of BMO, BMO-SOVs-375, and 2%A/BMO-SOVs-375 at 77 K, (d) Raman spectra of BMO, BMO-SOVs-375, 2%A/BMO-SOVs-375 and 2%A/BMO (PD).

To investigate the optical band gap and absorption properties of the as-obtained samples, the UV-vis DRS spectra were provided and the results were illustrated in Figure 6a and Figure S2. It can see clearly that the adsorption edge of pure BMO appears at around 470 nm. Interestingly, compared with pure BMO, the main absorption edge of BMO-SOVs-375 changes little. More importantly, the 2%A/BMO-SOVs-375 exhibits a significant enhancement of visible light absorption at 420-800 nm after treated by calcination as a result of the introduction of SOVs and metallic Ag nanoparticles. Furthermore, it can be found that 2%A/BMO-SOVs-375, 2%A/BMO-SOVs-375 (PD), and 2%A/BMO (PD) display a stronger absorption about 550 nm, which could be attributed to the strong SPR due to metallic Ag nanoparticles.^[27-29] From the inset of Figure 6a, the color changes a little from BMO to BMO-SOVs-375, consistent with the edge absorption observed. The color of powder

changes from pale yellow of BMO to gray of 2%A/BMO-SOVs-375, indicating the existence of metallic Ag.^[52] To prove the change of band gap structure, the band gap energy (E_g) of BMO, BMO-SOVs-375 and 2%A/BMO-SOVs-375 were calculated by plots of $(\alpha h\nu)^{1/2}$ versus energy ($h\nu$), and the results were illustrated in Figure 6b. It can be clearly observed that the E_g values of BMO, BMO-SOVs-375 and 2%A/BMO-SOVs-375 are about 2.45, 2.49 and 2.33 eV, respectively. The above results can be ascribed to the synergistic effect between SOVs and metallic Ag co-modification and coupling with BMO, which somehow improves the visible light response ability. Figure 6c shows the valence band X-ray photoelectron spectra (VB-XPS) of BMO and BMO-SOVs-375 photocatalysts. It can be seen that the positions of valence band (VB) of BMO and BMO-SOVs-375 are about 1.95 and 1.85 eV vs NHE, respectively. Meanwhile, the conduction band (CB) edges of BMO and BMO-SOVs-375 are calculated to be -0.50 and -0.64 eV, respectively, based on their band gaps. This result can be ascribed to the introduction of SOVs elevates the both conduction and valence bands. A similar phenomenon was also observed on BiOCl.^[53] According to the characterization findings, we can describe the band structure of BMO and BMO-SOVs-375 using a schematic diagram (Figure 6d).

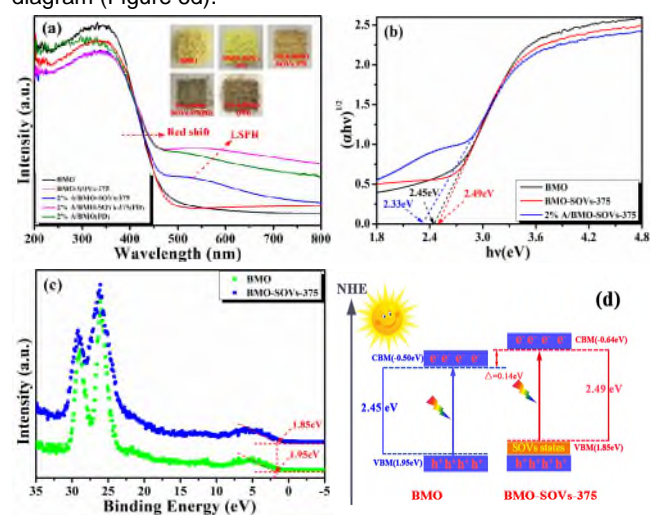


Figure 6. (a) UV-vis diffuse reflectance spectra of BMO, BMO-SOVs-375, 2%A/BMO-SOVs-375, 2%A/BMO-SOVs-375 (PD), and 2%A/BMO (PD) (insert: the color of the photocatalysts), (b) The band gap value estimated by the curve of $(\alpha h\nu)^{1/2}$ versus photon energy plotted, (c) Valence band XPS spectra, and (d) Schematic illustration of the band structures of BMO and BMO-SOVs-375, respectively.

Photocatalytic activity and degradation mechanism

To evaluate the photocatalytic activities of as-obtained samples, phenol was chosen as a representative organic pollutant for photocatalytic degradation. Figure 7a show the variation of phenol concentration (C/C_0) over BMO, BMO-SOVs-375, 2%A/BMO-SOVs-375, 2%A/BMO-SOVs-375 (PD), and 2%A/BMO (PD) photocatalysts against reaction time under visible light irradiation ($\lambda \geq 420$ nm). It can be clearly observed

that pure BMO exhibits 4.8% of phenol decrease efficiency after 180 min, and BMO-SOVs-375 and 2%A/BMO-SOVs-375 composites both displayed superior photocatalytic activities. Especially, for the 2%A/BMO-SOVs-375 exhibited the highest photocatalytic activity in the degradation of phenol compared to BMO, BMO-SOVs-375, 2%A/BMO-SOVs-375 (PD), and 2%A/BMO (PD). The improved photocatalytic activity of 2%A/BMO-SOVs-375 is attributed to the synergistic effect between the SOVs, metallic Ag and BMO, which not only improves the visible light response ability, but also utilizes the strong SPR effect in metallic Ag nanoparticles, promoting the efficient separation of photogenerated electron-hole pairs.

As shown in Figure 7b, the typical evolution of the absorption spectra of phenol with BMO, BMO-SOVs-375, and 2%A/BMO-SOVs-375 under visible light irradiation ($\lambda \geq 420$ nm). It was found that the characteristic absorption peak is observed at 507 nm at the beginning of photodegradation of phenol. With increasing irradiation time, the absorption peak of 2%A/BMO-SOVs-375 obviously decreases and virtually no peak could be observed after 180 min irradiation than pure BMO, in which slightly decreases. This result confirms that the complete photocatalytic degradation of phenol by 2%A/BMO-SOVs-375 during the irradiation.

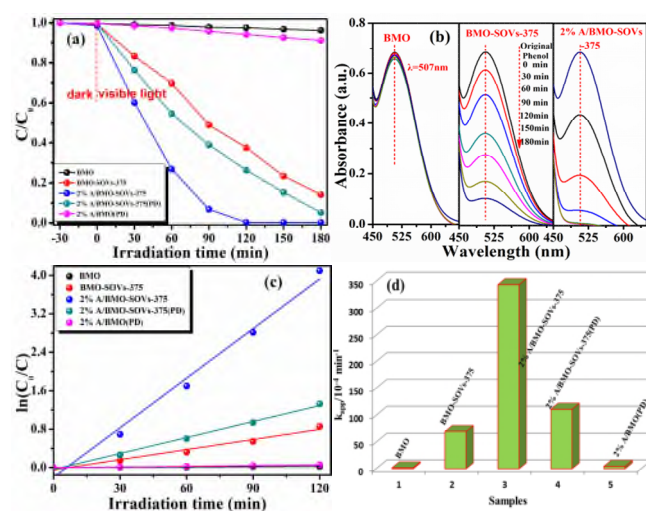
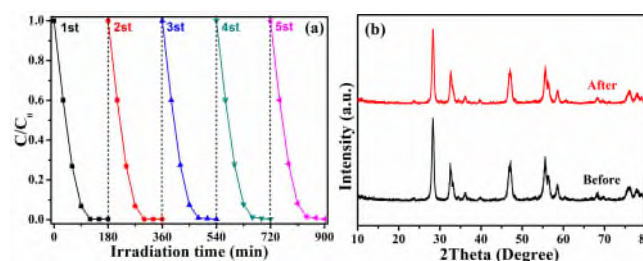


Figure 7. (a) Photocatalytic degradation efficiency of phenol by BMO, BMO-SOVs-375, 2%A/BMO-SOVs-375, 2%A/BMO-SOVs-375 (PD), and 2%A/BMO (PD), (b) The change of the absorption spectra of photodegraded phenol with increasing irradiation time under visible light using BMO, BMO-SOVs-375, and 2%A/BMO-SOVs-375 as catalysts, respectively, (c) Kinetic plot of C/C_0 versus irradiation time for the photodegradation of phenol with different catalysts, (d) The rate constants of the photodegradation of phenol using different catalysts.

In addition, the kinetic behaviors of as-obtained samples for photodegradation of phenol were investigated. It can see clearly that all of them fit well with the pseudo-first-order kinetics model^[54]: $\ln(C_0/C) = k_{app} \cdot t$, where k_{app} denotes the apparent rate constant (min^{-1}), C_0 represents the initial phenol concentration ($\text{mg} \cdot \text{L}^{-1}$) and C represents the final concentration of phenol in



solution after irradiation time t minute. Figure 7c illustrates the plot of $\ln(C_0/C)$ versus irradiation time (t), using BMO, BMO-SOVs-375, 2%A/BMO-SOVs-375, 2%A/BMO-SOVs-375 (PD), and 2%A/BMO (PD) photocatalysts. Figure 7d show the k_{app} values of as-obtained samples for photodegradation of phenol. The k_{app} values of BMO, BMO-SOVs-375, 2%A/BMO-SOVs-375, 2%A/BMO-SOVs-375 (PD), and 2%A/BMO (PD) are 1.88×10^{-4} , 70.3×10^{-4} , 343.9×10^{-4} , 111.2×10^{-4} , and $4.73 \times 10^{-4} \text{ min}^{-1}$, respectively. It can be found that the k_{app} values of 2%A/BMO-SOVs-375 is much higher than these samples, which is approximately 183 times higher than that of pure BMO. Simulated results of k_{app} for each process, in the presence of different photocatalysts with regard to phenol, were summarized in Table S1. The dramatically enhanced photocatalytic activity is attributed to the synergistic effect between the SOVs, metallic Ag and BMO, which not only improves the visible light response ability, but also utilizes the strong SPR effect in metallic Ag nanoparticles, promoting the efficient separation of photogenerated electron-hole pairs.

The variation of phenol concentration (C/C_0) photocatalysts against reaction time over 2%A/BMO-SOVs with different calcination temperatures for 2 h and different calcination time at 375 °C are shown in Figure S3a and S3b, respectively. With the increase of calcination temperature, the activity of the as-obtained samples first increases and then decreases and the activity of 2%A/BMO-SOVs calcinated at 375 °C is the best. As displayed in Figure S3b, with the increase of calcination time, the photocatalytic activities of 2%A/BMO-SOVs-375 samples slightly enhanced. These results indicate that the introduction of SOVs and SPR effect of metallic Ag nanoparticles due to controlled calcination temperatures act as pivotal roles for the enhanced photocatalytic performance.

Figure S3c illustrates the photocatalytic activities of the as-prepared A/BMO-SOVs-375 nanocomposites with different metallic Ag contents at 375 °C for 2h for the photocatalytic degradation of phenol under visible light irradiation. We can see that when the mole ratio of Ag increased from 0.5% to 2% in the composites, photocatalytic degradation efficiency of phenol was obviously improved. However, when the mole ratio of Ag was further increased to 5%, the photocatalytic activity decreased. It can be attributed to the the excessive amount of Ag nanoparticles on the surface acts as recombination center for photogenerated electrons and holes,^[16, 39] resulting in decreased photocatalytic performance.

To investigate the influence of different initial dosages of 2%A/BMO-SOVs-375 on the photocatalytic degradation efficiency, a series of experiments were performed and the results are shown in Figure S3d. It can be clearly observed that when the amount of 2%A/BMO-SOVs-375 was increased from 0.50 to 1.00 $\text{g} \cdot \text{L}^{-1}$, the degradation efficiency of phenol was improved accordingly, which is due to more active sites would be provided. However, when the amount of 2%A/BMO-SOVs-375 further increased and more than 1.00 $\text{g} \cdot \text{L}^{-1}$, the degradation rate would slightly decrease due to the scattering of light, and would severely reduce the intensity of light penetrating through the phenol solution.^[55]

From the viewpoint of practical application, it is of significant importance to investigate the stability of prepared 2%A/BMO-SOVs-375. Figure 8a illustrates five successive photocatalytic degradation experiments. It can see clearly that the photocatalytic performance shows a slight decrease after five cycles. In addition, the XRD patterns of 2%A/BMO-SOVs-375 samples before and after photodegradation of phenol were acquired and are shown in Figure 8b. It can be found that the crystal structure of the 2%A/BMO-SOVs-375 photocatalyst showed no obvious changes during the photocatalytic reaction. Consequently, the 2%A/BMO-SOVs-375 composite is a quite stable and reusable photocatalyst, which can be utilized to degrade organic pollutants during practical applications.

Figure 8. (a) Photocatalytic degradation of phenol with the 2%A/BMO-SOVs-375 sample for five cycles, (b) XRD patterns of the 2%A/BMO-SOVs-375 samples before and after photodegradation of phenol under visible light irradiation ($\lambda \geq 420 \text{ nm}$).

In addition, 4-NP was used as the second model pollutant to further evaluate the visible light photocatalytic performance of the as-prepared samples, and the results are displayed in Figure 9. Figure 9a illustrates the variation of 4-NP concentration (C/C_0) over BMO, BMO-SOVs-375, 2%A/BMO-SOVs-375, 2%A/BMO-SOVs-375 (PD), and 2%A/BMO (PD) photocatalysts against reaction time under light irradiation ($\lambda \geq 420 \text{ nm}$). It can be easily seen that the 2%A/BMO-SOVs-375 exhibited the highest photocatalytic activity in the degradation of 4-NP compared to those photocatalysts, which is in good agreement with the photocatalytic degradation of phenol experiments results. Figure 9b illustrates the typical evolution of the absorption spectra of 4-NP with 2%A/BMO-SOVs-375 under visible light irradiation ($\lambda \geq 420 \text{ nm}$). It is obvious that the main band of 4-NP at 318 nm decreased monotonously with irradiation time, indicating that 4-NP was photodegraded.

Figure 9c illustrates the photocatalytic degradation curves of 4-NP in the form of $\ln(C_0/C)$ versus irradiation time (t), using BMO, BMO-SOVs-375, 2%A/BMO-SOVs-375, 2%A/BMO-SOVs-375 (PD), and 2%A/BMO (PD) photocatalysts. Figure 9d shows the k_{app} values of as-obtained samples for photodegradation of 4-NP. It can be easily seen that the k_{app} values of 2%A/BMO-SOVs-375 is much higher than these samples, which is approximately 27 times higher than that of pure BMO. Simulated results of k_{app} for each process, in the presence of different photocatalysts with regard to 4-NP, are summarized in Table S1. The remarkable photodegradation performance is attributed to the synergistic effect between the SOVs, metallic Ag and BMO, which not only improves the visible light response ability, but also utilizes the strong SPR effect in metallic Ag nanoparticles, promoting the efficient separation of photogenerated electron-hole pairs. This result is in good accordance with that the photocatalytic degradation of phenol experiments results.

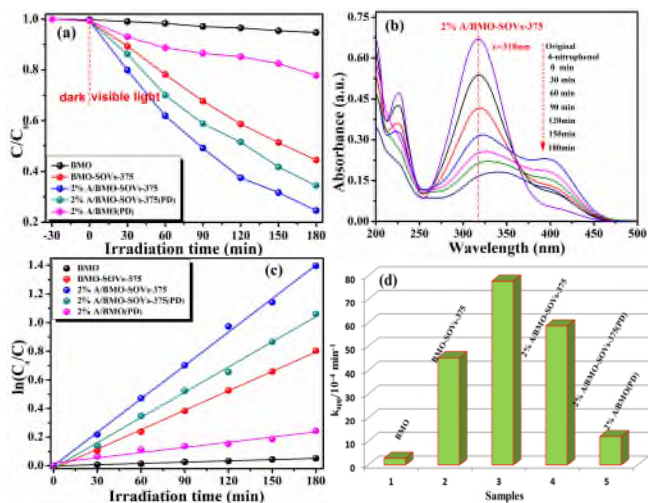


Figure 9. (a) photocatalytic degradation efficiency of 4-NP by BMO, BMO-SOVs-375, 2%A/BMO-SOVs-375, 2%A/BMO-SOVs-375 (PD), and 2%A/BMO (PD), (b) The change of the absorption spectra of photodegraded 4-NP with increasing irradiation time under visible light using 2%A/BMO-SOVs-375 as a catalyst, respectively, (c) Kinetic plot of C/C_0 versus irradiation time for the photodegradation of 4-NP with different catalysts, (d) The rate constants of the photodegradation of 4-NP using different catalysts.

To further evaluate the mineralization rate of phenol and 4-NP over BMO and 2%A/BMO-SOVs-375, TOC analysis were carried out, which monitored the concentration of remained organic substance in the aqueous solution and the degree of mineralization can be calculated that is displayed in Figure 10. It can be observed that 57.1 % and 48.7% of carbon contents in phenol and 4-NP were eliminated in the presence of 2%A/BMO-SOVs-375, which was much higher than that of BMO (2.5% and 4.7%), further indicating the enhanced photocatalytic performance. It should also be noted that 2%A/BMO-SOVs-375 shows higher photocatalytic and mineralization performances toward phenol and 4-NP, which is again attributed to the synergistic effect between the SOVs, metallic Ag and BMO.

In order to investigate the generation, transfer, and recombination of photogenerated electron-hole pairs on the semiconductor,^[56] PL emission spectra was recorded and the results are shown in Figure 11a. Recent results revealed that the higher intensity means the higher rate of photogenerated electron and hole recombination.^[57] It is clear that 2%A/BMO-SOVs-375 exhibits the lowest PL signal in comparison with BMO and BMO-SOVs-375, suggesting that the recombination rate of photoinduced electron-hole pairs was efficiently inhibited via the modification of SOVs and metallic Ag nanoparticles on the surface of BMO. This effect can be further confirmed by the TR-PL analysis. Moreover, a blue-shift in the PL emission peak of 2%A/BMO-SOVs-375 was observed comparison with BMO, which could be mainly attributed to the recombination of the photogenerated holes with the single electron oxygen vacancy.^[37, 58, 59] This result is in good accordance with TEM, EPR, Raman and UV-vis analysis.

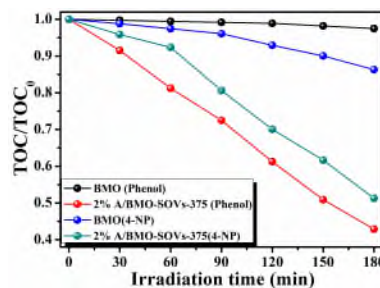
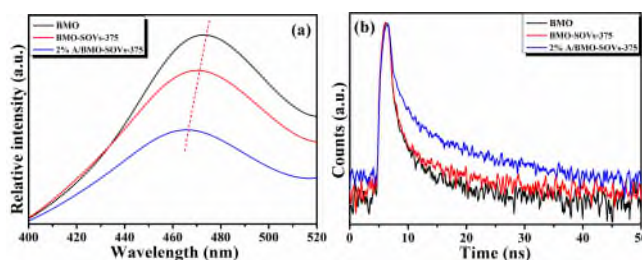


Figure 10. TOC measurement during mineralisation of phenol and 4-NP over BMO and 2%A/BMO-SOVs-375 composites under visible light illumination ($\lambda \geq 420$ nm).

Additionally, to further confirm the recombination process of photogenerated electron and hole pairs, time-resolved PL decay spectra were performed (Figure 11b). These spectra are in good agreement with the two-exponential decay models,^[14] and the fitting results are shown in Table S2. As shown in Figure 11b and Table S2, the lifetime of 2%A/BMO-SOVs-375 is 13.09 ns, which is much longer than that of BMO (i.e., 3.39 ns) and BMO-SOVs-375 (i.e., 4.36 ns), respectively. The prolonged lifetime is attributed to the synergistic effect between SOVs and metallic Ag nanoparticles, which effectively accelerates the separation of photogenerated electron and hole. The results are in



accordance with the observation from the PL measurements.

Figure 11. (a) Photoluminescence spectra, (b) Time-resolved fluorescence decay spectra of BMO, BMO-SOVs and 2%A/BMO-SOVs-375.

To further investigate the underlying mechanism of the excellent photocatalytic activities of 2%A/BMO-SOVs-375, active species trapping experiments were carried out. In this study, ethylenediaminetetraacetic acid disodium salt (EDTA-2Na), benzoquinone (BQ), and isopropanol (IPA) were applied as the scavengers of holes (h^+) superoxide radicals ($\cdot O_2^-$) and hydroxyl radicals ($\cdot OH$), respectively.^[60] Figure 12 illustrates the active species trapping experiments in photocatalytic degradation of phenol with 2%A/BMO-SOVs-375. The experimental results show that the addition of EDTA-2Na slightly hindered the photocatalytic activity, while the addition of BQ and IPA largely suppressed the photocatalytic degradation efficiency of phenol. Thus, it could be inferred that $\cdot O_2^-$ and $\cdot OH$ were the main reaction species in the phenol photodegradation process over A/BMO-SOVs.

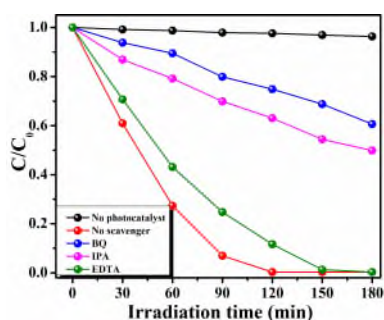
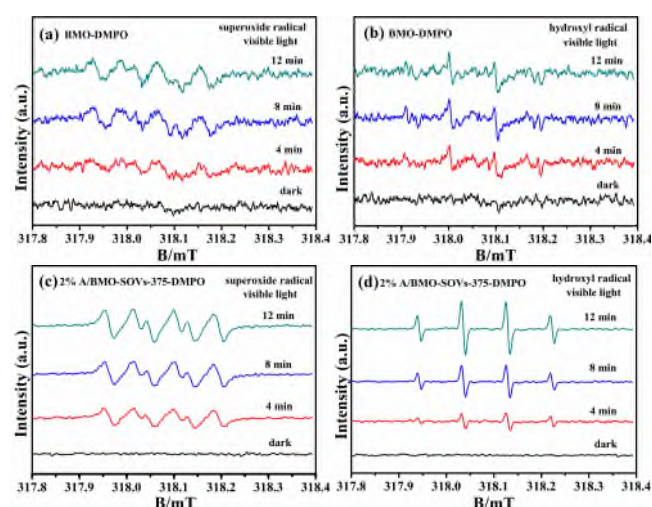


Figure 12. Kinetic curves of the 2%/BMO-SOVs-375 composite on the degradation of phenol in the presence of different radical scavengers under



visible light irradiation ($\lambda \geq 420$ nm).

Figure 13. DMPO spin-trapping ESR spectra of (a) BMO and (c) 2%/BMO-SOVs-375 in methanol dispersion for $\text{DMPO}\cdot\text{O}_2^-$, DMPO spin-trapping ESR spectra of (b) BMO and (d) 2%/BMO-SOVs-375 in aqueous dispersion for $\text{DMPO}\cdot\text{OH}$.

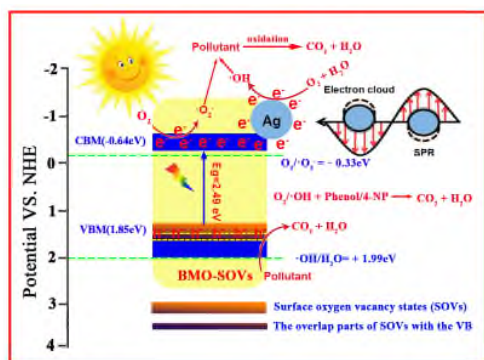
To further verify the presence of $\cdot\text{OH}$ and $\cdot\text{O}_2^-$ radicals in the photocatalytic reaction systems, the spin-trapping ESR technique was carried out,^[61, 62] and the results were shown in Figure 13 and Figure S4. Experiment was first conducted under dark condition and visible light irradiation of 4 min, 8 min, and 12 min. Figure 13 and Figure S4 shows the results of BMO, BMO-SOVs-375, and 2%/BMO-SOVs-375. It can be clearly observed that the characteriW the light was on, the $\cdot\text{O}_2^-$ and $\cdot\text{OH}$ radicals signals could be observed, further confirming the forming of $\cdot\text{O}_2^-$ and $\cdot\text{OH}$ during the photodegradation process. As shown in Figure 13a and 13b, BMO shows very weak the $\cdot\text{O}_2^-$ and $\cdot\text{OH}$ radicals signals, indicating that the $\cdot\text{O}_2^-$ and $\cdot\text{OH}$ were barely generated in the photocatalysis process. However, for 2%/BMO-SOVs-375, the intensity of radical signals gradually enhanced as the irradiation time prolonged (Figure 13c

and 13d). After visible light irradiation for 12 min, the special spectrum with relative intensities of 1 : 1 : 1 : 1 quartet signal was clearly observed, which is characteristic of $\text{DMPO}\cdot\text{O}_2^-$ adduct.^[63] Meanwhile, the $\cdot\text{OH}$ radical was captured to form $\text{DMPO}\cdot\text{OH}$ adduct with relative intensities of 1 : 2 : 2 : 1 quadruplet signal.^[64, 65] The ESR results indicate that $\cdot\text{O}_2^-$ and $\cdot\text{OH}$ radicals are both produced over 2%/BMO-SOVs-375, which is in good agreement with the active species trapping experimental results. Figure S4 shows the $\text{DMPO}\cdot\text{O}_2^-$ and $\text{DMPO}\cdot\text{OH}$ characteristic peaks of BMO-SOVs-375. Sample BMO-SOVs-375 shows a highly intensive $\cdot\text{O}_2^-$ and $\cdot\text{OH}$ radical signals compared to those of BMO under visible light irradiation.

On the basis of the above semiconductor band structure analysis and the ESR results, the remarkable photocatalytic performance of the 2%/BMO-SOVs-375 photocatalysts may be attributed to the synergistic effect of SOVs and metallic Ag nanoparticles, and the possible photocatalytic mechanism describing the charge transfer and separation process is proposed in Scheme 2. According to the results reported by Zhu et al.,^[66] the SOV is a shallow defect, which may be near the conduction band minimum (CBM) or above the valence band maximum (VBM). As manifested in our previous works, the existence of SOVs would induce the formation of sub-bands above VB.^[40] A similar phenomenon has also been observed on $\text{Bi}_2\text{O}_2\text{CO}_3$, BiPO_4 and BiFeO_3 .^[26, 66, 67] Our experimental results show that BMO-SOVs-375 photocatalytic performance is evidently increased compared with pure BMO, which is attributed to the efficient separation of photogenerated electron-hole pairs and transfer.^[66] Furthermore, when metallic Ag nanoparticles are deposited on BMO-SOVs-375 surface, due to the Fermi level equilibrium between BMO and Ag nanoparticles, Schottky barriers formed at a metal-semiconductor junction.^[68, 69] This unique metal-semiconductor interface allows only the movement of electrons from the semiconductor to metal particles and hinders electron transfer back across the Schottky barrier, and thereby preventing from the recombination of the photogenerated electron-hole pairs.^[40] Therefore, the resulting 2%/BMO-SOVs-375 photocatalyst shows a very high photocatalytic activity via a synergetic effect of SOVs and metallic Ag nanoparticles. Consequently, the enhanced photocatalytic activity for phenol and 4-NP degradation with 2%/BMO-SOVs-375 could be explained as follows.

Under visible light irradiation, the BMO-SOVs-375 can be excited to generate photoexcited electron-hole pairs.. Subsequently, the electrons from the CB of BMO-SOVs-375 flow into metallic Ag nanoparticles surface due to a Schottky barrier at the metal-semiconductor interface,^[70] and thus reducing the recombination possibility with photogenerated holes, which was confirmed by the PL and TR-PL spectra (Figure 11). The photogenerated electrons could react with the dissolved oxygen molecules (O_2) from the environment to generate $\cdot\text{O}_2^-$ radicals, while the valence holes photogenerated on the surface of BMO-SOVs-375 could not react with OH^- or H_2O molecules to form $\cdot\text{OH}$ radicals, which can ascribed to the reason that the photo-induced hole (h^+) of BMO-SOVs-375 (1.85 eV vs. NHE) is more negative than that of $\cdot\text{OH}/\text{OH}^-$ potential (1.99 eV vs NHE, pH = 7).^[71] Nevertheless, the typical characteristic peaks of $\text{DMPO}\cdot$

$\cdot\text{OH}$ adducts (Figure 13d and Figure S4b) were also observed, indicating that the $\cdot\text{OH}$ radicals are also produced in both BMO-SOVs-375 and 2%A/BMO-SOVs-375 reaction systems. It is believed that the observed $\cdot\text{OH}$ radicals originate from the further reduction of $\cdot\text{O}_2^-$ via $\cdot\text{O}_2^- \rightarrow \text{H}_2\text{O}_2 \rightarrow \cdot\text{OH}$.^[72, 73] Meanwhile, the phenol and 4-NP molecules can be directly degraded by the strong oxidizing holes (h^+) from the VB of BMO. It has been reported that both $\cdot\text{OH}$ and $\cdot\text{O}_2^-$ have strong oxidation capacity, which can mineralize phenol and 4-NP to H_2O , CO_2 and other inorganic anions (Figure 10). Hence, the 2%A/BMO-SOVs-375 exhibits the highest visible light responsive photocatalytic performance, which can be attributed to the synergistic effect between the SOVs, metallic Ag nanoparticles and BMO. This synergistic effect not only improves the visible light absorption ability, but also produces the SPR effect and Schottky barriers, greatly promoting the efficient separation of photogenerated electron-hole pairs and resulting in the very high photocatalytic performance.



Scheme 2. Schematic illustration of hole-electron separation and transfer process for the 2%A/BMO-SOVs-375 photocatalysts under visible light irradiation ($\lambda \geq 420$ nm).

Conclusions

In summary, novel A/BMO-SOVs photocatalysts were successfully fabricated via a reliable solvothermal methods followed by a mild impregnation-calcination treatment. TEM, EPR, and Raman spectra analyses results confirmed the co-existence of SOVs, metallic Ag nanoparticles and BMO after controlled calcination process. The 2%A/BMO-SOVs-375 showed the optimal efficiency of phenol and 4-NP degradation under visible light irradiation, achieving about 100% and 80% degradation of these organic substance within 180 min, respectively, and the k_{app} are 183 and 26.5 times higher than that of pure BMO. The reason for the remarkable photocatalytic activity is reasonably attributed to the synergistic effect between the SOVs, metallic Ag nanoparticles and BMO. These results were further demonstrated by 57.1 % and 48.7 removal efficiency of phenol and 4-NP by TOC measurement, respectively. This heterojunction not only improves the visible light absorption, but also produces the SPR effect and Schottky barriers, which significantly promote the separation of photogenerated electrons and holes, and simultaneously

suppresses the recombination of electrons and holes, thus resulting in the high photocatalytic performance on 2%A/BMO-SOVs-375. In addition, this work provides an effective strategy for the design and fabrication of highly efficient photocatalysts through integrating SOVs and SPR metallic Ag nanoparticles and the potential to other environment pollutants' removal.

Experimental Section

Synthesis of photocatalysts

Preparation of Bi_2MoO_6 (BMO). All the chemicals were analytical grade and used as received. Distilled water was used in all experiments. The pure Bi_2MoO_6 was synthesized according to our previous work.^[40] In brief, 1.3 mmol of $\text{Bi}(\text{NO}_3)_3 \cdot 5\text{H}_2\text{O}$ and 0.65 mmol of $\text{Na}_2\text{MoO}_4 \cdot 2\text{H}_2\text{O}$ were dissolved in 13.0 mL of ethylene glycol (EG) under vigorously stirring. Afterwards, 32.5 mL of ethanol was added and the colourless solution was stirred for another 30 min at room temperature. Finally, the miscible solution was transferred into a 65.0 mL Teflon-lined stainless steel autoclave, which was maintained at 160 °C for 12 h under autogenous pressure. After completion of the reaction, the autoclave naturally cooled down to room temperature. The resulting precipitates were collected and washed with ethanol and deionized water for three times and then dried at 60 °C for 12 h in a vacuum oven. The obtained product was marked as BMO.

Synthesis of oxygen vacancy-rich $\text{Ag}/\text{Bi}_2\text{MoO}_6$ (A/BMO-SOVs) photocatalysts. The A/BMO-SOVs composite photocatalysts were prepared through a facile impregnation-calcination method. First, 0.61 g pure BMO powders were dispersed into 60 mL aqueous solution that containing various amount of AgNO_3 (10^{-3} g·mL⁻¹) in a beaker under vigorous stirring. Then, the suspension was stirred vigorously at 70 °C to evaporate the water. After that, the precipitates were calcined at 300 °C, 350 °C, 375 °C, 400 °C, 425 °C and 450 °C in air-rich atmosphere with the heating rate of 2°C/min for 2 h in the muffle furnace to obtain the final A/BMO-SOVs composite. The products were denoted as 2%A/BMO-SOVs-X (X=300 °C, 350 °C, 375 °C, 400 °C, 425 °C, 450 °C). Following the similar procedure, we fixed calcination temperature at 375 °C and controlled the molar ratio of Ag nanoparticles deposit on BMO-SOVs at 0.5%, 1%, 2%, 3% and 5%, respectively. The obtained samples were denoted as Y%A/BMO-SOVs-375 (Y = 0, 0.5, 1, 2, 3, 5). In addition, to investigate the effect of calcination time on the photocatalytic activities on the series 2%A/BMO-SOVs-375 photocatalysts, we fixed the calcination temperatures at 375 °C and changed the calcination time to 1h, 2h, 3h and 5h, respectively. The resulted products were denoted as 2%A/BMO-SOVs-Z (Z = 1h, 2h, 3h, 5h). The preparation process of A/BMO-SOVs composite is shown in **Scheme 1**.

For comparison, two control samples were also prepared according to our previous work.^[40] Briefly, 1.0 mmol of the pure BMO (BMO-SOVs) and a certain amount of AgNO_3 solution (3.5 mL, 10^{-3} g·mL⁻¹) were added into 20 mL of deionized water under stirring. The suspension was stirred for 30 min in the dark, and then irradiated at ambient temperature for 2 h using a 400W xenon lamp under stirring. During the irradiation, the supernatant was collected and tested until Ag^+ was precipitated completely. After completed photoreduction process, the samples were collected, washed with water to completely remove NO_3^- ions, and finally dried at 60 °C for 12 h in a vacuum oven. The theoretical deposited amount of Ag is 2% to pure BMO (BMO-SOVs), and the resulted sample were denoted as 2%A/BMO (PD) and 2%A/BMO-SOVs-375 (PD), respectively. Herein A/BMO-SOVs indicates that Ag nanoparticles was

deposited on the surface of oxygen vacancy-rich Bi₂MoO₆ photocatalysts via a impregnation-calcination treatment, while A/BMO-SOVs (PD) means that Ag nanoparticles was deposited on the surface of oxygen vacancy-rich Bi₂MoO₆ photocatalysts via a photoreduction process

Characterization of photocatalysts

Powder X-ray diffraction (XRD) was carried out on a Shimadzu XRD-7000 X-ray diffractometer using Cu K α radiation ($\lambda = 0.15418$ nm) at a scanning rate of 2° min⁻¹ in a 2 θ range of 10° - 80°. The accelerating voltage and the applied current were 40 kV and 30 mA, respectively. X-ray photoelectron spectroscopy (XPS) was recorded on a PHI-5400 X-ray photoelectron spectrometer. Field emission scanning electron microscope (FE-SEM) images were recorded on a JSM-6700F scanning electron microscope. Energy-dispersive X-ray (EDS) spectra were obtained using a JEOL-2100 at an accelerating voltage of 200 kV. High-resolution transmission electron microscope (HRTEM) images was recorded on a JEM-2100 electron microscope operated at an accelerating voltage of 200 kV. In situ electron paramagnetic resonance (EPR) measurement was took in an Endor spectrometer (JEOL ES-ED3X). The g factor was obtained by taking the signal of manganese as standard. The electron spin resonance (ESR) signals of radicals spin-trapped by spin-trap reagent DMPO (5, 5'-dimethyl-1-pyrroline-N-oxide) (Sigma Chemical Co.) in water were examined on a Bruker model ESR JES-FA200 spectrometer equipped with a quanta-Ray Nd: YAG laser system as the irradiation source ($\lambda > 410$ nm). To minimize experimental errors, the same type of quartz capillary tube was used for all ESR measurements. Raman spectra were recorded by using a Horiba Jobin-Yvon LabRam HR800 Raman microspectrometer, with laser excitation at 320 nm. The UV-Vis diffuse reflectance spectra (UV-Vis-DRS) of the samples were obtained using Shimadzu UV-2550 UV-Vis spectrophotometer. BaSO₄ was used as a reflectance standard. Room-temperature photoluminescence spectra (PL) and time-resolved photoluminescence spectra (TR-PL) were detected with a Horiba FLTCSPC fluorescence spectrophotometer.

Measurements of photocatalytic activity

Phenol and 4-NP were used as probe organic pollutants to assess the photocatalytic activities. A 400W halogen lamp (Nanjing XuJiang electrical and mechanical plant, Nanjing, P. R. China) with a 420 nm cutoff filter was chosen as the visible light source. The suspension containing 200 mg of photocatalyst and 200 mL of 10 mg·L⁻¹ phenol or 4-NP (1.0 g_{cat}/L_{solution}) fresh aqueous solution were continuously stirred in the dark for 30 min to establish an adsorption/desorption equilibrium of phenol or 4-NP solution. After this period of time, the light source was turned on. During the reaction, 5.0 mL of samples were taken at given time intervals and the photocatalysts were then separated by centrifugation. The residual concentration of phenol in solution was estimated using absorption at 507 nm by a Shimadzu 2550 UV-visible spectrophotometer following the 4-aminoantipyrine colorimetric method. The remaining concentration of 4-NP was monitored using a Shimadzu 2550 UV-visible spectrophotometer at the wavelength of 318 nm. Total organic carbon (TOC) in the phenol solution was recorded by automatic total organic carbon analyzer (VARIO, Elementar, Germany).

Acknowledgements

This work was supported by the National Natural Science Foundation of China (No. 21663030, 21666039) and the Project of Science & Technology Office of Shaanxi Province (No.

2018TSCXL-NY-02-01, 2015SF291) and Natural Science Program of the Education Department of Shaanxi Province (No. 15JS119).

Keywords: Oxygen vacancy-rich Ag/Bi₂MoO₆ • Surface oxygen vacancy • Surface plasmon resonance • Synergistic effect • Phenol and 4-nitrophenol degradation

- [1] Z.G. Yi, J.H. Ye, N. Kikugawa, T. Kako, S.X. Ouyang, H.S. Williams, H. Yang, J.Y. Cao, W.J. Luo, Z.S. Li, Y. Liu, R.L. Withers, *Nat. Mater.* 2010, 9, 559-564.
- [2] S. J. A. Moniz, J. Tang, *ChemCatChem*, 2015, 7, 1659-1667..
- [3] H.L. Wang, L.S. Zhang, Z.G. Chen, J.Q. Hu, S.J. Li, Z.H. Wang, J.S. Liu, X.C. Wang, *Chem. Soc. Rev.* 2014, 43, 5234-5244.
- [4] D.J. Martin, G.G. Liu, S.J.A. Moniz, Y.P. Bi, A.M. Beale, J.H. Ye, J.W. Tang, *Chem. Soc. Rev.* 2015, 44, 7808-7828.
- [5] W.J. Ong, L.L. Tan, Y.H. Ng, S.T. Yong, S.P. Chai, *Chem. Rev.* 2016, 116, 7159-7329.
- [6] Y.H. Li, K.L. Lv, W.K. Ho, F. Dong, X.F. Wu, Y. Xia, *Appl. Catal. B: Environ.* 2017, 202, 611-619.
- [7] Y. Ma, Y.L. Jia, Z.B. Jiao, M. Yang, Y.X. Qi, Y.P. Bi, *Chem. Commun.* 2015, 51, 6655-6658.
- [8] Z. Dai, F. Qin, H.P. Zhao, F. Tian, Y.L. Liu, R. Chen, *Nanoscale* 2015, 7, 11991-11999.
- [9] D.J. Wang, H.D. Shen, L. Guo, F. Fu, Y.C. Liang, *New J. Chem.* 2016, 40, 8614-8624.
- [10] C.S. Guo, J. Xu, S.F. Wang, L. Li, Y. Zhang, X.C. Li, *CrystEngComm* 2012, 14, 3602-3608.
- [11] G.H. Tian, Y.J. Chen, W. Zhou, K. Pan, Y.Z. Dong, C.G. Tian, H.G. Fu, *J. Mater. Chem.* 2011, 21, 887-892.
- [12] S. Yuan, Y. Zhao, W.B. Chen, C. Wu, X.Y. Wang, L.N. Zhang, Q. Wang, *ACS Appl. Mater. Interfaces* 2017, 9, 21781-21790.
- [13] Y. Zheng, T.F. Zhou, X.D. Zhao, W.K. Pang, H. Gao, S.A. Li, Z. Zhou, H.K. Liu, Z.P. Guo, *Adv. Mater.* 2017, 29, 1700396-1700404.
- [14] X.L. Wu, J.N. Hart, X.M. Wen, L. Wang, Y. Du, S.X. Dou, Y.H. Ng, R. Amal, J. Scott, *ACS Appl. Mater. Interfaces* 2018, 10, 9342-9352.
- [15] J.L. Lv, J.F. Zhang, J. Liu, Z. Li, K. Dai, C.H. Liang, *ACS Sustainable Chem. Eng.* 2018, 6, 696-706.
- [16] X.C. Meng, Z.S. Zhang, *Appl. Catal. B: Environ.* 2017, 209, 383-393.
- [17] X.X. Chang, T. Wang, P. Zhang, J.J. Zhang, A. Li, J.L. Gong, *J. Am. Chem. Soc.* 2015, 137, 8356-8359.
- [18] Z. Dai, F. Qin, H.P. Zhao, J. Ding, Y.L. Liu, R. Chen, *ACS Catal.* 2016, 6, 3180-3192.
- [19] G.M. Wang, Y.C. Ling, Y. Li, *Nanoscale* 2012, 4, 6682-6691.
- [20] J. Liao, L. Chen, M. Sun, B. Lei, X. Zeng, Y. Sun, F. Dong, *Chin. J. Catal.* 2018, 4, 779-789
- [21] M.L. Guan, C. Xiao, J. Zhang, S.J. Fan, R. An, Q.M. Cheng, J.F. Xie, M. Zhou, B.J. Ye, Y. Xie, *J. Am. Chem. Soc.* 2013, 135, 10411-10417.
- [22] Y.Y. Zhu, Q. Ling, Y.F. Liu, H. Wang, Y.F. Zhu, *Appl. Catal. B: Environ.* 2016, 187, 204-211.
- [23] J. Ding, Z. Dai, F. Qin, H.P. Zhao, S. Zhao, R. Chen, *Appl. Catal. B: Environ.* 2017, 205, 281-291.
- [24] J. Ding, Z. Dai, F. Tian, B. Zhou, B. Zhao, H.P. Zhao, Z.Q. Chen, Y.L. Liu, R. Chen, *J. Mater. Chem. A* 2017, 5, 23453-23459.
- [25] Y.H. Lv, Y.F. Liu, Y.Y. Zhu, Y.F. Zhu, *J. Mater. Chem. A* 2014, 2, 1174-1182.
- [26] S.X. Yu, Y.H. Zhang, F. Dong, M. Li, T.R. Zhang, H.W. Huang, *Appl. Catal. B: Environ.* 2018, 226, 441-450.
- [27] M. Rycenga, C.M. Cobley, J. Zeng, W.Y. Li, C.H. Moran, Q. Zhang, D. Qin, Y.N. Xia, *Chem. Rev.* 2011, 111, 3669-3712.
- [28] Y.G. Sun, *Chem. Soc. Rev.* 2013, 42, 2497-2511.
- [29] Z.W. Seh, S.H. Liu, M.C. Low, S.Y. Zhang, Z.L. Liu, A. Mlayah, M.Y. Han, *Adv. Mater.* 2012, 24, 2310-2314.

-
- [30] V. Vaianoa, M. Matarangolola, J.J. Murciab, H. Rojasb, J.A. Navíoc, M.C. Hidalgo, *Appl. Catal. B: Environ.* 2018, 225, 197-206.
- [31] Y.Y. Bu, Z.Y. Chen, W.B. Li, *Appl. Catal. B: Environ.* 2014, 144, 622-630.
- [32] X.X. Chen, Y.P. Li, X.Y. Pan, D. Cortie, X.T. Huang, Z.G. Yi, *Nat. Commun.* 2016, 7, 12273-12281.
- [33] L.L. Wang, M. Yu, C.L. Wu, N. Deng, C. Wang, X.Q. Yao, *Adv. Synth. Catal.* 2016, 358, 2631-2641.
- [34] J. Di, J.X. Xia, M.X. Ji, B. Wang, S. Yin, Y. Huang, Z.G. Chen, H.M. Li, *Appl. Catal. B: Environ.* 2016, 188, 376-387.
- [35] X.N. Wang, R. Long, D. Liu, D. Yang, C.M. Wang, Y.J. Xiong, *Nano Energy* 2016, 24, 87-93.
- [36] C.C. Li, T. Wang, Z.J. Zhao, W.M. Yang, J.F. Li, A. Li, Z.L. Yang, G.A. Ozin, J.L. Gong, *Angew. Chem. Int. Ed.* 2018, 19, 5376-5380.
- [37] Y.Y. Duan, M. Zhang, L. Wang, F. Wang, L.P. Yang, X.Y. Li, C.Y. Wang, *Appl. Catal. B: Environ.* 2017, 204, 67-77.
- [38] J.W. Wan, W.X. Chen, C.Y. Jia, L.R. Zheng, J.C. Dong, X.S. Zheng, Y. Wang, W.S. Yan, C. Chen, Q. Peng, D.S. Wang, Y.D. Li, *Adv. Mater.* 2018, 30, 1705369-1705377.
- [39] Y.C. Deng, L. Tang, G.M. Zeng, C.Y. Feng, H.R. Dong, J.J. Wang, H.P. Feng, Y.N. Liu, Y.Y. Zhou, Y. Pang, *Environ. Sci.: Nano* 2017, 4, 1494-1511.
- [40] D.J. Wang, H.D. Shen, L. Guo, C. Wang, F. Fu, Y.C. Liang, *Appl. Surf. Sci.* 2018, 436, 536-547.
- [41] Y.S. Xu, W.D. Zhang, *Dalton Trans.* 2013, 42, 1094-1101.
- [42] Y.H. Lv, W.Q. Yao, R.L. Zong, Y.F. Zhu, *Sci. Rep.* 2016, 6, 19347.
- [43] H.Y. Mou, C.X. Song, Y.H. Zhou, B. Zhang, D.B. Wang, *Appl. Catal. B: Environ.* 2018, 221, 565-573.
- [44] H.P. Li, J.Y. Liu, W.G. Hou, N. Du, R.J. Zhang, X.T. Tao, *Appl. Catal. B: Environ.* 2014, 160-161, 89-97.
- [45] C. Zhang, Y.F. Zhu, *Chem. Mater.* 2005, 17, 3537-3545.
- [46] J.G. Hou, S.Y. Cao, Y.Z. Wu, F. Liang, Y.F. Sun, Z.S. Lin, L.C. Sun, *Nano Energy* 2017, 32, 359-366.
- [47] W.T. Bi, C.M. Ye, C. Xiao, W. Tong, X.D. Zhang, W. Shao, Y. Xie, *Small* 2014, 10, 2820-2825.
- [48] H. Li, J. Li, Z.H. Ai, F.L. Jia, L.Z. Zhang, *Angew. Chem. Int. Ed.* 2018, 57, 122-138.
- [49] X.B. Zhang, L. Zhang, J.S. Hu, X.H. Huang, *RSC Adv.* 2016, 6, 32349-32357.
- [50] Y.C. Miao, G.F. Pan, Y.N. Huo, H.X. Li, *Dyes Pigment.* 2013, 99, 382-389.
- [51] Z. Wei, Y.F. Liu, J. Wang, R.L. Zong, W.Q. Yao, J. Wang, Y.F. Zhu, *Nanoscale* 2015, 7, 13943-13950.
- [52] Y.Z. Wang, X.Y. Huang, K.Q. Wang, L.L. Zhang, B. Wang, Z.B. Fang, Y. Zhao, F. Gao, P. Liu, W.H. Feng, *J. Mater. Chem. A* 2018, 6, 9200-9208.
- [53] Z.Y. Ma, P.H. Li, L.Q. Ye, Y. Zhou, F.Y. Su, C.H. Ding, H.Q. Xie, Y. Bai, P.K. Wong, *J. Mater. Chem. A* 2017, 5, 24995-25004.
- [54] C.W. Tan, G.Q. Zhu, M. Hojamberdiev, K. Okada, J. Liang, X.C. Luo, P. Liu, *Appl. Catal. B: Environ.* 2014, 152-153, 425-436.
- [55] T. Yan, Q. Yan, X.D. Wang, H.Y. Liu, M.M. Li, S.X. Lu, W.G. Xu, M. Sun, *Dalton Trans.* 2015, 44, 1601-1611.
- [56] X. Feng, W.D. Zhang, Y.J. Sun, H.W. Huang, F. Dong, *Environ. Sci.: Nano* 2017, 4, 604-612.
- [57] Z.F. Jiang, W.M. Wan, W. Wei, K.M. Chen, H.M. Li, P.K. Wong, J.M. Xie, *Appl. Catal. B: Environ.* 2017, 204, 283-295.
- [58] F.C. Lei, Y.F. Sun, K.T. Liu, S. Gao, L. Liang, B.C. Pan, Y. Xie, *J. Am. Chem. Soc.* 2014, 136, 6826-6829.
- [59] G.S. Huang, X.L. Wu, Y.F. Mei, X.F. Shao, G.G. Siu, *J. Appl. Phys.*, 2003, 93, 582-585.
- [60] L.Q. Jing, Y.G. Xu, S.Q. Huang, M. Xie, M.Q. He, H. Xu, H.M. Li, Q. Zhang, *Appl. Catal. B: Environ.* 2016, 199, 11-22.
- [61] J.J. Yang, D.M. Chen, Y. Zhu, Y.M. Zhang, Y.F. Zhu, *Appl. Catal. B: Environ.* 2017, 205, 228-237.
- [62] H.W. Huang, X.W. Li, J.J. Wang, F. Dong, P.K. Chu, T.R. Zhang, Y.H. Zhang, *ACS Catal.* 2015, 5, 4094-4103.
- [63] W.W. He, H.M. Jia, W.G. Wamer, Z. Zheng, P.J. Li, J.H. Callahan, J.J. Yin, *J. Catal.* 2014, 320, 97-105.
- [64] P.X. Qiu, C.M. Xu, H. Chen, F. Jiang, X. Wang, R.F. Lu, X.R. Zhang, *Appl. Catal. B: Environ.* 2017, 206, 319-327.
- [65] P.H. Shao, Z.J. Ren, J.Y. Tian, S.S. Gao, X.B. Luo, W.X. Shi, B.Y. Yan, J. Li, F.Y. Cui, *Chem. Eng. J.* 2017, 323, 64-73.
- [66] Y.H. Lv, Y.Y. Zhu, Y.F. Zhu, *J. Phys. Chem. C* 2013, 117, 18520-18528.
- [67] D. Chen, F. Niu, L.S. Qin, S. Wang, N. Zhang, Y.X. Huang, *Sol. Energy Mater. Sol. Cells* 2017, 171, 24-32.
- [68] Q.J. Xiang, J.G. Yu, B. Cheng, H.C. Ong, *Chem. Asian J.* 2010, 5, 1466-1474.
- [69] L.G. Devi, R. Kavitha, *Appl. Surf. Sci.* 2016, 360, 601-622.
- [70] B. Yuan, C.H. Wang, Y. Qi, X.L. Song, K. Mu, P. Guo, L.T. Meng, H.M. Xi, *Colloids and Surfaces A: Physicochem. Eng. Aspects* 2013, 425, 99-107.
- [71] X.L. Hu, J. Tian, Y.J. Xue, Y.J. Li, H.Z. Cui, *ChemCatChem* 2017, 9, 1511-1516.
- [72] X. Ding, K. Zhao, L.Z. Zhang, *Environ. Sci. Technol.* 2014, 48, 5823-5831.
- [73] Z.F. Jia, F.M. Wang, F. Xin, B.Q. Zhang, *Ind. Eng. Chem. Res.* 2011, 50, 6688-6694.
-